RSC Advances

PAPER

View Article Online
View Journal | View Issue

Cite this: *RSC Adv.*, 2019, **9**, 36717

Rapid synthesis of $MgCo_2O_4$ and $Mg_{2/3}Ni_{4/3}O_2$ nanocrystals in supercritical fluid for Mg-ion batteries

Quang Duc Truong, *[a] Hiroaki Kobayashi [b] and Itaru Honma*[b]

Received 30th June 2019
Accepted 2nd November 2019

DOI: 10.1039/c9ra04936c

rsc.li/rsc-advances

Magnesium metal complex oxides are potential electrode materials for magnesium ion batteries with high specific capacities. However, the strong electrostatic interaction between Mg^{2+} and the host lattice due to its divalency induces slow intercalation kinetics of Mg ions within the crystal lattices. Thus, nanocrystalline particles with shortened Mg ion diffusion distance enable the insertion/extraction of Mg ions and improve the specific capacities of the batteries. Herein, we report the facile rapid production of crystalline $MgCo_2O_4$ and $Mg_{2/3}Ni_{4/3}O_2$ nanocrystals by rapid supercritical fluid processing. The phase transition from spinel to rocksalt during the Mg^{2+} ion intercalation has been confirmed by high-resolution transmission electron microscopy. The nanosheets of $Mg_{2/3}Ni_{4/3}O_2$ rocksalt nanocrystals were controllably synthesized for the first time, which are active materials for magnesium-ion batteries.

1. Introduction

Advanced rechargeable batteries are crucial for development of renewable energy and addressing the growing energy consumption and also play a central role in fulfilling the requirements of emerging autonomous electronic devices. Battery technologies based on multivalent-ions, such as Mg, Ca, Al, with high volumetric energy density are particularly attractive for large-scale energy-storage applications,[1–4] in which Mg-ion batteries have been considered as promising beyond Li-ion technology. However, due to the divalence of Mg, exploring novel stable electrolytes with reversible metal stripping/deposition and searching for higher voltage cathodes materials are still challenging for the development of Mg-ion batteries.[5–11] Great efforts have been made to explore electrode materials with high-capacity, high cell voltage and resulting high energy density. In this context, two transition metals, Ni and Co, have been used as the electroactive elements in almost all Li-ion cathode materials, including layered-rocksalt cathode materials in the $Li(Ni,Mn,Co)O_2$ form, and the promising automotive industry Ni-rich materials. Thus, it is expected that Mg–M–O complex oxides of Co and Ni will play a crucial role in the development of Mg-ion batteries with higher energy density. Yet there has been little improvement due to multiple limitation including their modest capacity, low voltage, self-discharge, irreversible Mg insertion, and instability toward electrolytes.

Controlling size, shape, morphology and facet growth has been shown to improve the electrochemical performance of various Li/Mg–M–O complex oxides. Morphology-controlled spinel-type MgM_2O_4 (M = Fe, Mn, Co, Ni) have been considered as effective method to reach their theoretical capacity of 270 mA h g^{-1} and high operating voltage.[12–15] For example, $MgMn_2O_4$ with nanosized or hollow spheres morphologies exhibited a high reversible capacity exceeding 220 mA h g^{-1} at a voltage of approximately 2.4 V *vs.* Mg.[16–18] $MgCr_2O_4$ nanoparticles synthesized by continuous hydrothermal flow synthesis method at high temperature demonstrates an initial capacity of 271 mA h g^{-1}.[19] Designing them at small particle sizes would shorten bulk diffusion lengths and maximize sites for cathode/electrolyte transfer of Mg^{2+}, thereby further facilitating electrochemical performance.[19] However, the reproducible and scalable fabrication of Mg–M–O complex oxides in controlled manner, is challenging using conventional synthesis methods. Recently, supercritical fluid (SCF) process has been applied for the production of high-quality, high-yield, inorganic nanosheets and electrode material for energy storage applications in our group.[20–23] This rapid and facile one-pot synthetic method resulted in a highly active materials with unique morphological control. In previous report, we applied our method for the synthesis of olivine-type $MgMnSiO_4$ and $MgCoSiO_4$ nanoparticles *via* rapid supercritical fluid processing at low temperature.[24] Here, we show a shape-controlled synthesis of complex metal oxides, which involves the direct one-pot nucleation and growth of fine nanocrystals of spinel $MgCo_2O_4$ and rocksalt $Mg_{2/3}Ni_{4/3}O_2$ by the SCF water. The obtained $MgCo_2O_4$ and $Mg_{2/3}Ni_{4/3}O_2$ nanocrystals exhibited the

---

[a] *Ceramics and Biomaterials Research Group, Advanced Institute of Materials Science, Ton Duc Thang University, Ho Chi Minh City, Vietnam. E-mail: truongquangduc@tdtu.edu.vn*

[b] *Institute of Multidisciplinary Research for Advanced Materials, Tohoku University, Katahira, 2-1-1, Aobaku, Sendai 980-8577, Japan. E-mail: itaru.honma.e8@tohoku.ac.jp*

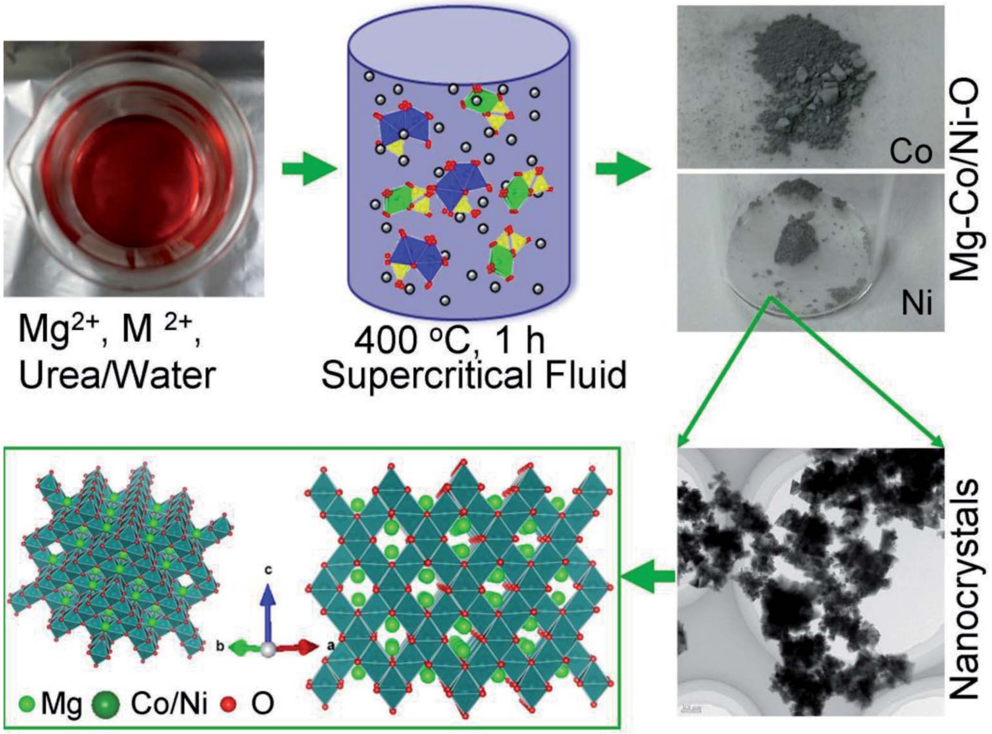

Scheme 1 The synthesis of Mg–M–O complex oxides by supercritical fluid processing. Schematic illustration of the crystal growth in supercritical water and their crystallographic orientation.

specific capacities of 81.0 and 69.8 mA h g^{-1}, respectively, at a current rate of C/50 (5.4 mA g^{-1}) in Mg-ion batteries.

2. Experimental section

2.1 Synthesis method

Mg–M–O complex oxides were directly synthesized by one-pot supercritical fluid (SCF) method with a reaction time of 30 minutes.[20–24] Typically, 1 mmol nitrates solutions ($Mg(NO_3)_2 \cdot 6H_2O$) were mixed with 2 mmol $Co(NO_3)_2 \cdot 4H_2O$ or $Ni(NO_3)_2 \cdot 6H_2O$, (Wako, Japan) solutions in total volume of 5 ml H_2O. The solution was heated at 60 °C with continuous stirring, followed by addition of 3 mmol urea (CH_4N_2O, Wako, Japan). The obtained colored solutions were heated with continuous stirring at 60 °C for 15 minutes then 5 ml each solution was transferred to a 10 ml batch reactor and heated at 400 °C for 30 minutes. After which, reactors were allowed to cool to room temperature by water quenching. The resultant powder was separated by centrifugation and washed with distilled water and ethanol. Finally, the obtained specimen was dried at 60 °C in vacuum for 1 day (Scheme 1).

2.2 Material characterization

The crystal structures of the SCF products were checked by powder X-ray diffraction (XRD; Bruker AXS D8 Advance, 40 kV and 30 mA) with CuKα radiation (λ = 1.5406 Å). Data were collected in the 2θ–θ scanning mode with a scan speed of 4° min^{-1} and a step size of 0.02°. Scanning electron microscopy (SEM) images were observed on an Hitachi S-4800 field-emission SEM. Transmission electron microscopy (TEM) and high-resolution TEM (HRTEM) images were observed on Hitachi H7650 and High Resolution TEM (TOPCOM EM-002B) with an acceleration voltage of 200 kV. X-ray photoelectron spectroscopy (XPS) measurements were carried using a ULVAC PHI 500 (Versa Probe II) equipped with a monochromatic Al K$_\alpha$ (1486.6 eV) X-ray source. The photoelectrons signals were collected in the constant pass energy mode using a concentric hemispherical energy analyser that was calibrated with pure gold, silver, and copper standard samples by setting the Au 4f$_{7/2}$, Ag 3d$_{5/2}$, and Cu 2p$_{3/2}$ peaks at binding energies of 83.96 ± 0.02 eV, 368.21 ± 0.02 eV, and 932.62 ± 0.02 eV, respectively. Charge referencing was corrected using the adventitious hydrocarbon at binding energy of 284.6 eV. Quantitative analysis of the XPS spectra was carried out using a Shirley background subtraction before performing a least-square-error fit with a mixture of Gaussian and Lorentzian line shapes.

2.3 Electrochemical measurement

The electrochemical performance of Mg–M–O was investigated using CR2032 type coin cells (CR2032).[25] The working electrodes are composed of 80 wt% Mg–M–O, 10 wt% PTFE (poly(tetrafluoroethylene)) as a binder and 10 wt% acetylene black. These materials were ground by conventional agar mortar to make electrode paste. The prepared paste was spread uniformly, rolling into sheet then dried in a vacuum oven for 4 h at 160 °C. The cathode sheet was punched into circular discs and cut into wafers (7 mm in diameter, 0.025 mm in thickness, 1 mg). The

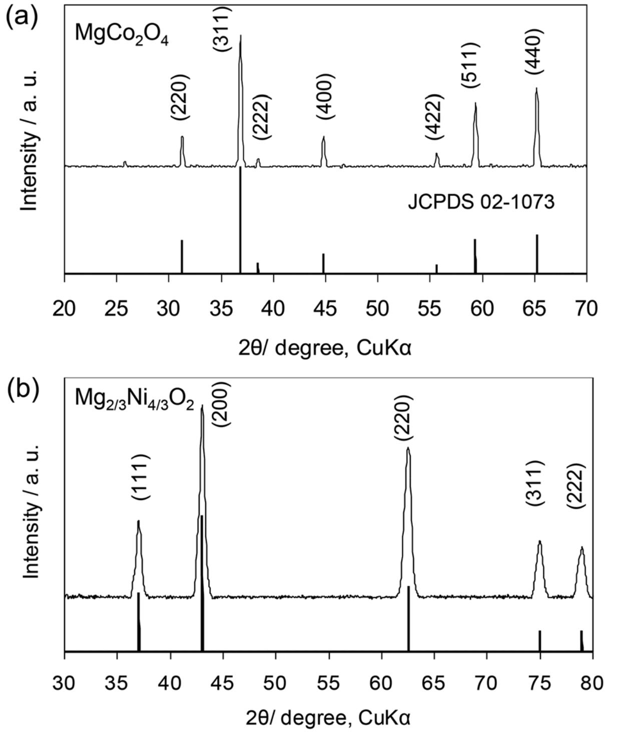

Fig. 1 XRD patterns of the (a) $MgCo_2O_4$ and (b) $Mg_{2/3}Ni_{4/3}O_2$ synthesized by supercritical water processing.

capacitive anode was prepared by mixing of 80 wt% Maxsorb MSC-30, 10 wt% PTFE as a binder and 10 wt% acetylene black.[26–28] The tested cell was assembled inside an argon-filled glove box. The cathode and anode electrodes were separated by a microporous polypropylene film. The electrolyte consists the solution of 0.5 mol L^{-1} $Mg(ClO_4)_2$ in acetonitrile C_2H_3N or 1.0 mol L^{-1} magnesium bis(trifluoromethylsulfonyl)amide ($Mg(TFSA)_2$) or ($Mg[N(SO_2CF_3)_2]_2$) in adiponitrile $C_6H_8N_2$. The charge–discharge cycling were performed galvanostatically between −0.5 and 1.0 V or −1.5 and 1.0 V *versus* C on multi-channel battery testers (Hokuto Denko, Japan) at charge/discharge rate of C/50. Current densities and specific capacities were calculated on the basis of the weight of Mg–M–O cathode in the electrode. Cyclic voltammetry measurements were performed at 1 mV s using Solartron analytical potentiostat.

3. Results and discussion

3.1 Characterization of Mg–M–O nanoparticles

The formation mechanism of the spinel and rocksalt metal complex oxides in supercritical fluid condition is schematically depicted in Scheme 1. Upon the rapid heating of the supercritical fluid processing, the supersaturation of reactant species led to the precipitation of Mg–M–O seeds and further growth into small nanocrystals.[20–24] Urea played an important role as *in situ* pH controlling agent. pH of solutions is determined to be 9.0. We assume that pH is important factor for precipitation of spinel and rocksalt during the supercritical fluid treatment. The phase purity of metal complex oxides was examined by X-ray diffraction (XRD) investigation (Fig. 1). The XRD patterns of the synthesized nanocrystals exhibited diffraction patterns that could be index to cubic spinel structure of $MgCo_2O_4$ (space group $Fd\bar{3}m$, a = 8.10 Å) with minor impurity and rocksalt $Mg_xNi_{1-x}O_2$ (space group $Fm\bar{3}m$, a = 4.195 Å). In the case of $Mg_{2/3}Ni_{4/3}O_2$ sample, we initially try to synthesize spinel-type $MgNi_2O_4$, but it forms rocksalt structure. The molecular formula of $Mg_xNi_{1-x}O_2$ was determined to be $Mg_{2/3}Ni_{4/3}O_2$ because we use the molar ratio of Mg/Ni = 0.5.

A typical $MgCo_2O_4$ nanocrystals was characterized by FESEM, TEM, selected area electron diffraction and HRTEM. It can be seen from Fig. 2a and b, the $MgCo_2O_4$ nanocrystals exhibit a mainly nanocubic shape with size less than 300 nm. TEM characterization in Fig. 2c and d clearly revealed the

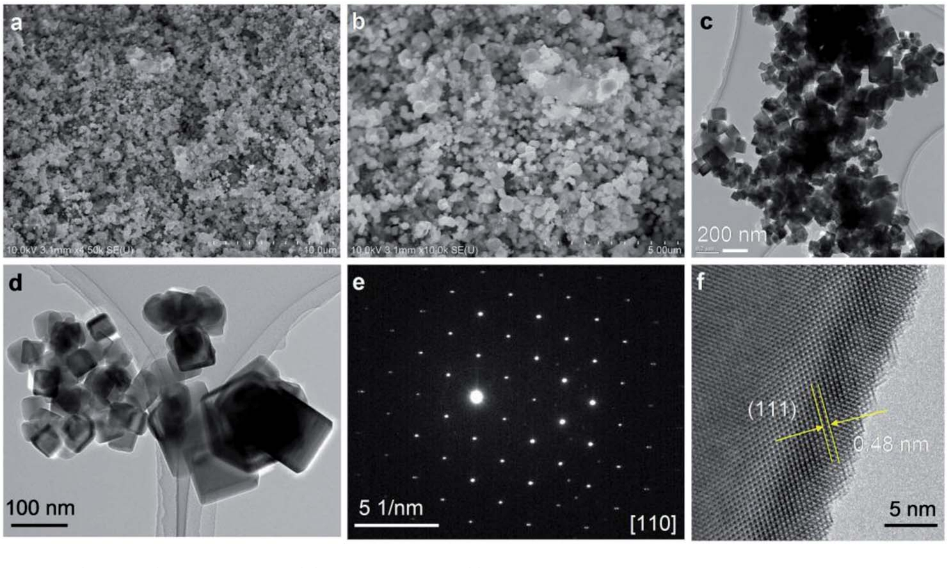

Fig. 2 (a and b) SEM images; (c and d) TEM images; (e) SAED pattern, (f) HRTEM image of $MgCo_2O_4$ synthesized by supercritical fluid water at 400 °C.

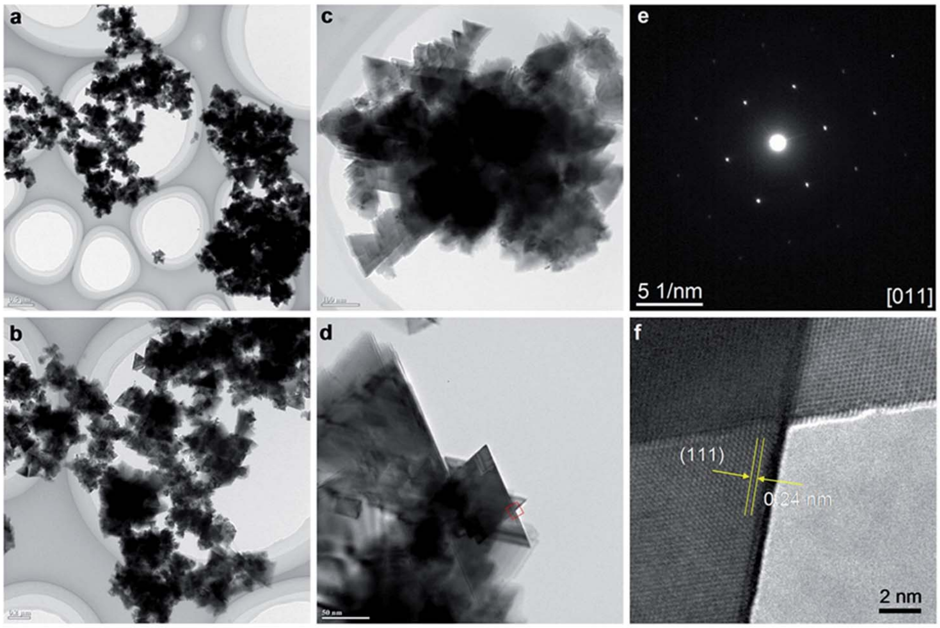

Fig. 3 (a–d) TEM images; (e) SAED pattern, (f) HRTEM image of $Mg_{2/3}Ni_{4/3}O_2$ synthesized by supercritical fluid processing.

nanocrystals with cubic shapes and well-facets characteristic. The crystallinity and the growth direction of nanocrystals was studied by the SAED pattern as displayed in Fig. 2c. SAED pattern consists of spots pattern, indicating the single-crystalline nature of the nanocrystal. The pattern can be indexed to the [110] zone axis of cubic spinel. The crystal lattice spacing of 4.8 Å, shown in the HRTEM image in Fig. 2f, corresponds to the (111) lattice planes, indicating the successful growth of cubic structure.

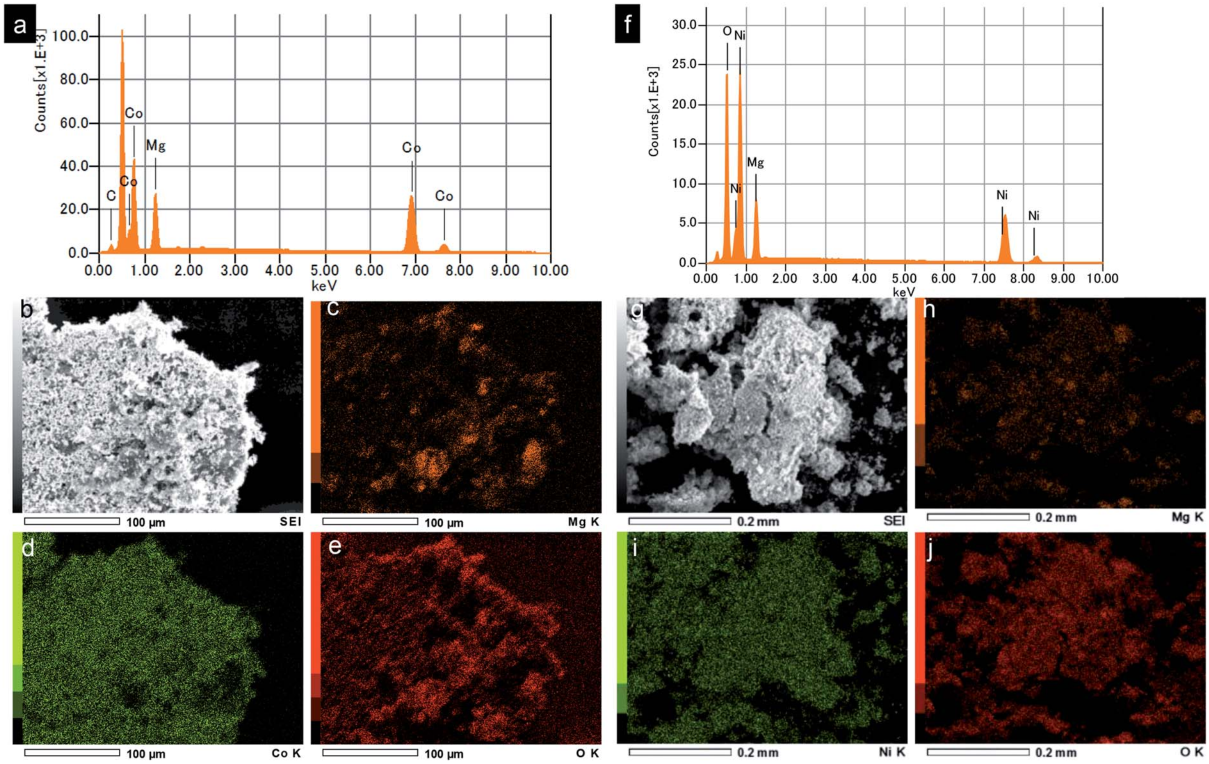

Fig. 4 (a and f) EDS spectra, (b and g) SEM images and (c–e and h–j) elemental mapping of the synthesized $MgCo_2O_4$ and $Mg_{2/3}Ni_{4/3}O_2$ nanoparticles, respectively (C is from substrate).

The structural and phase purity characterization of the synthesized $Mg_{2/3}Ni_{4/3}O_2$ materials is provided in Fig. 3. TEM images of the obtained $Mg_{2/3}Ni_{4/3}O_2$ particles clearly indicate the presence of the hierarchical structures comprising of multiple triangle sheet branches (Fig. 3a and b). TEM images in Fig. 3c and d of nanocrystals demonstrate the triangle nanosheets of which the ripple-contrast revealed their ultrathin property. The Fig. 3e shows SAED pattern of the selected nanocrystal in Fig. 3d, corresponding to the [011] zone axis of the cubic rocksalt structure. Fig. 3f shows HRTEM image taken in a portion of particle in Fig. 3d. The lattice spacing of 0.24 nm can be assigned to {111} crystal planes (Fig. 3f), indicating that the nanoparticles are well-crystalline in rocksalt framework. The thin nanosheet structure of rocksalt $Mg_{2/3}Ni_{4/3}O_2$ is expected to show good electrochemical properties due to a shortening of Mg ion diffusion distance, fast charge and mass transport as well as enhancing the contact with the electrolyte and the resulting reaction kinetics.

Energy dispersive X-ray spectroscopy (EDS) analysis and elemental mapping were further studied to reveal the chemical compositions of the obtained nanocrystals. EDS spectrum of the $MgCo_2O_4$ sample shows the characteristic peaks of Mg, CO, O, which is consistent with the $MgCo_2O_4$ phase purity. The elements Mg, Co, O were found to be distributed uniformly in the entire sample as seen in EDS elemental mappings by SEM. Fig. 4f–j show results from EDS analysis and elemental mapping of $Mg_{2/3}Ni_{4/3}O_2$. Characterization results from XRD, SEM, TEM, EDS prove the formation of spinel $MgCo_2O_4$ and rocksalt $Mg_{2/3}Ni_{4/3}O_2$ by supercritical fluid water.

In addition, X-ray photoelectron spectroscopy (XPS) analysis was performed for the synthesized $MgCo_2O_4$ nanocrystals (Fig. 5a and b). The scan survey shows the presence of Mg, Co, O with the stoichiometry of Mg/Co ~1/2. Co 2p peak has significantly split spin–orbit components, $2p_{3/2}$ and $2p_{1/2}$, with Δ_{metal} = 15.3 eV. The cobalt signal can be seen at 779.6 eV with satellite structure at 6.2 eV higher similar to those in $LiCoO_2$, suggesting the presence of Co(III).[29] XPS analysis for $Mg_{2/3}Ni_{4/3}O_2$ can be found in Fig. 5c and d. The binding energy of Ni $2p_{3/2}$ at 853.4 eV is consistent with that of Ni^{2+}, showing that the oxidation state of nickel is 2+.[30] The spin–orbit split peaks for Ni 2p is observed with separation of 17.3 eV.

3.2 Electrochemical performance of $MgCo_2O_4$ and $Mg_{2/3}Ni_{4/3}O_2$ nanocrystals

The electrochemical properties of synthesized $MgCo_2O_4$ and $Mg_{2/3}Ni_{4/3}O_2$ materials were evaluated by using as cathode materials for magnesium ion batteries. The electrochemical

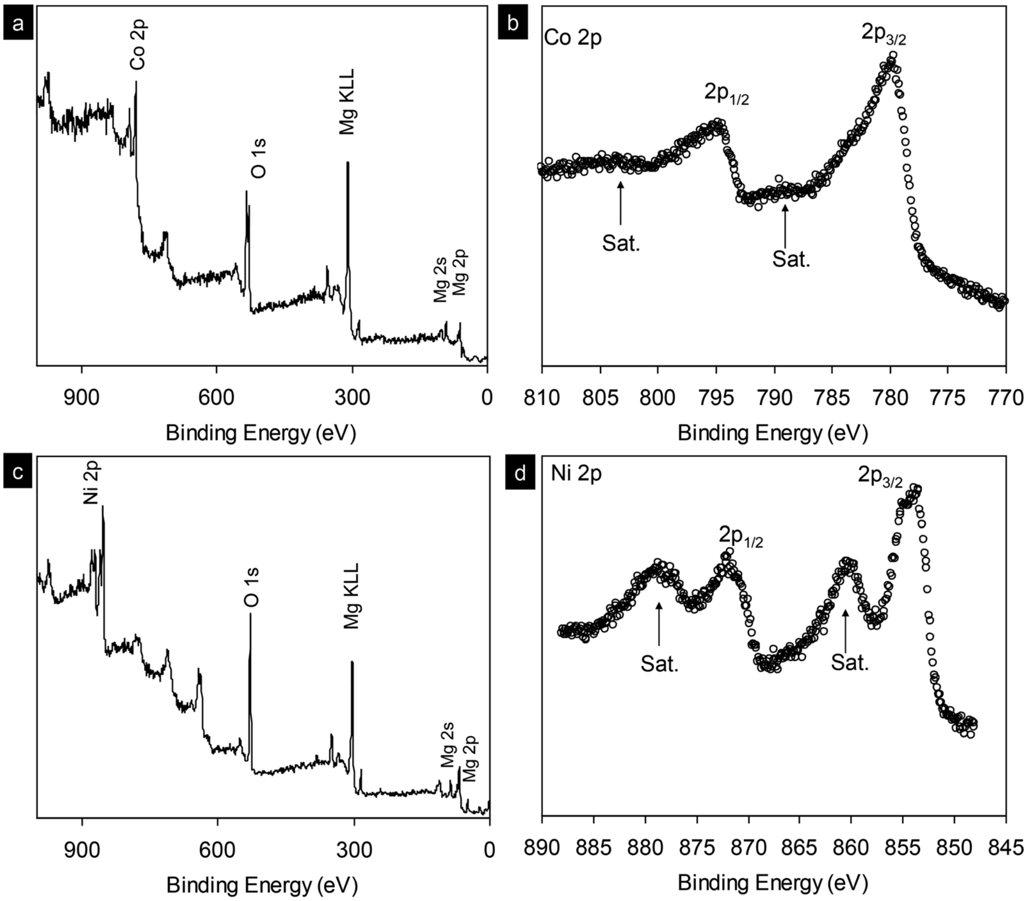

Fig. 5 (a and c) X-ray photoelectron spectrum survey scan of as-synthesized $MgCo_2O_4$ and $Mg_{2/3}Ni_{4/3}O_2$ nanocrystals. (b and d) High resolution scans for Co 2p and Ni 2p core levels, respectively.

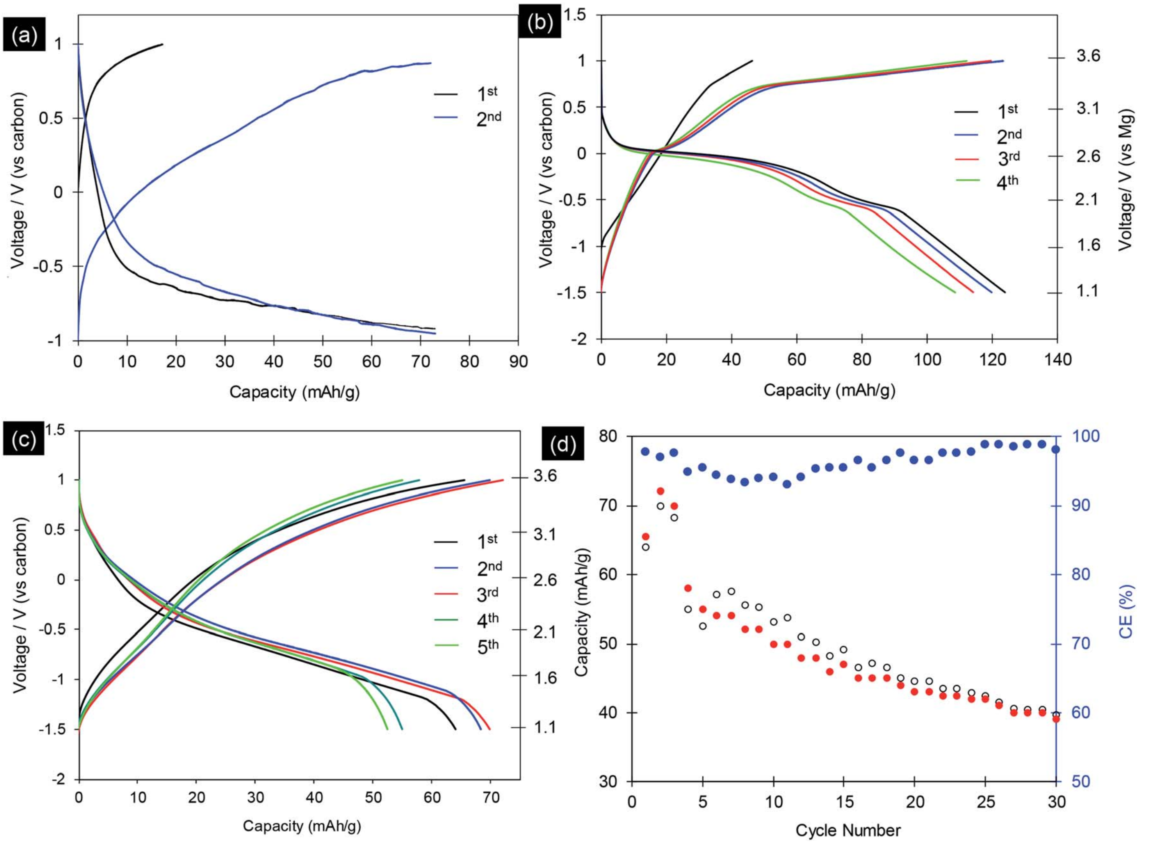

Fig. 6 (a and b) Electrochemical performances of the synthesized $MgCo_2O_4$ nanocrystals in Mg-ion batteries with Maxsorb MSC-30 nanoporous carbon on stainless steel as the anode and with 0.5 M $Mg(ClO_4)_2$ in ACN; 1 M ($Mg(TFSA)_2$) or ($Mg[N(SO_2CF_3)_2]_2$) in adiponitrile as the electrolytes, respectively, at current rate of C/50. (c) Typical charge/discharge profiles of $Mg_{2/3}Ni_{4/3}O_2$ nanocrystals at current rate of C/50 tested with Maxsorb MSC-30 as counter/reference electrodes and with 1 M ($Mg(TFSA)_2$) in adiponitrile as the electrolyte; (d) charge/discharge capacity of 30 cycles and corresponding coulombic efficiency (CE).

experiments for Mg-ion battery were performed in coin-cell type (CR2032) on multi-channel battery testers (Hokuto Denko, Japan) as reported elsewhere.[24,25,28] $MgCo_2O_4$ and $Mg_{2/3}Ni_{4/3}O_2$ were used as cathode by mixing with acetylene black (10 wt%) and PTFE binder (10 wt%). We first tested the three-electrode Mg-ion cells with $MgCo_2O_4$ cathode, Maxsorb MSC-30 nanoporous activated carbon as counter and quasi-reference electrode (QRE) and 0.5 M $Mg(ClO_4)_2$ in acetonitrile as electrolyte. The activated carbon is enable of reversible charge transport *via* double-layer capacitance (EDLC) due to its high surface area.[26–28] The cells were first charged. Fig. 6a shows typical charge/discharge profiles of $MgCo_2O_4$ nanoparticles at different cycles with current rate of C/50. The profiles clearly show an increase in potential from 2.6 to 3.6 V and 2.0 to 3.6 V *vs.* Mg/Mg^{2+} with a charge capacity of 17.3 and 70.1 mA h g^{-1} in first and second cycles, respectively. The discharge profiles show fast drop from 3.6 to 2.1 V with capacities of 73.1 and 73.2 mA h g^{-1} at the first and second cycles, respectively. The slow drop in the voltage window −0.8 to −1.0 V with capacities of 10–13 mA h g^{-1} was presumably attributed to surface reaction or decomposition of electrolytes. The first charge profiles indicate that 0.065 Mg ions per formula unit can be deintercalated from the spinel $MgCo_2O_4$ framework. However, the electrode presented a discharge capacities of 73.1 mA h g^{-1} which indicate the insertion of Mg into spinel to form rocksalt phases as reported elsewhere: $MgCo_2O_4 + Mg^{2+} + 2e \leftrightarrow Mg_2Co_2O_4$.[31–36]

Next we used 1.0 mol L^{-1} magnesium bis(trifluoromethylsulfonyl)amide ($Mg(TFSA)_2$) in adiponitrile as electrolyte. The electrochemical experiment was carried out at 70 °C, both voltage and charge/discharge capacities were improved. The initial charge/discharge voltage profiles of $MgCo_2O_4$ nanocrystals at current rate of C/50 are shown in Fig. 6b. The profiles show charge capacities of 46.3 and 124.1 mA h g^{-1} in first and second cycles, respectively. The $MgCo_2O_4$ materials delivered 125.1 and 119.3 mA h g^{-1} at the first and second discharge cycles, respectively. This capacity could be measured up to 10 cycles with continuous decrease. The specific capacities of $MgCo_2O_4$ obtained in this study are comparable to $MgCo_2O_4$ materials synthesized by inverse co-precipitation method,[31–36] with the same electrochemical experiment condition.[36] However, the obtained $MgCo_2O_4$ showed clear charge voltage curve. Ichitsubo and Idemoto *et al.* synthesized spinel materials, MgM_2O_4 (M = Fe, Mn, Co, Cr), by inverse co-precipitation method with annealing at 500 °C.[31–36] The specific capacities of 97 to 200 mA h g^{-1} were obtained, which are strongly depend on the temperature of

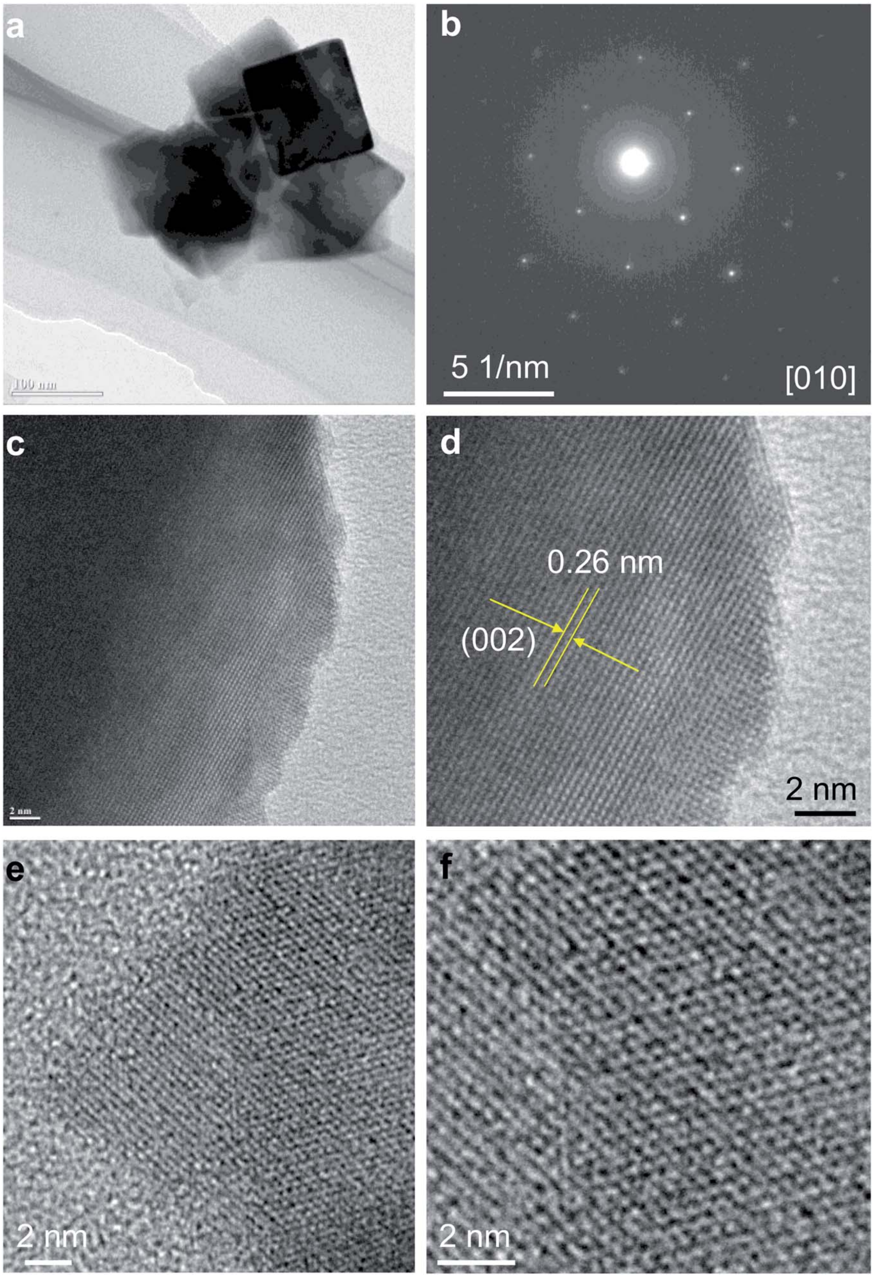

Fig. 7 (a) TEM images; (b) SAED pattern; (c and d) HRTEM images viewed from [010] direction; (e and f) HRTEM images viewed from [011] direction of electrochemically discharged sample $Mg_2Co_2O_4$.

electrochemical test (90 to 150 °C). Thus, the synthetic methods and the resulting particles size, morphologies play a crucial role in the determining performance of magnesium metal oxides in Mg-ion batteries.

We further examined the discharge particles by HRTEM to reveal the structure change. The cathode sample was disassembled in the glovebox and washed with acetonitrile. The morphologies and phase transition in charged sample was investigated in detail, and the result is shown in Fig. 7. TEM images of the discharge particles clearly indicates the presence of the cubic shape nanocrystals, which is unchange from original sample (Fig. 7a). The Fig. 7b shows SAED pattern of the selected nanocrystal in Fig. 7a, corresponding to the [010] zone axis of the cubic rocksalt structure. HRTEM images in Fig. 7c and d of the nanocrystals indicate the particle was viewed from [010] direction. Fig. 7d shows HRTEM image with lattice spacing of 0.26 and 0.28 nm, which can be assigned to {002} and {100} crystal planes, respectively, indicating that the nanocrystal are well transformed into cubic rocksalt. HRTEM images viewed from [011] direction are shown in Fig. 7e and f. Based on the electrochemical data and various spectroscopy method, Ichitsubo and Idemoto *et al.* have confirmed the insertion of Mg into spinel to form rocksalt during the discharge.[31–36] It is expected that Mg cations can be inserted onto 16c vacant sites in the spinel lattice to form Mg-rich rocksalt structure.[31–36] Our HRTEM analyses indicate reversible extraction and insertion of Mg-ion into $MgCo_2O_4$, with the structural feature of the discharge particles can be analyzed unambitiously.

We also studied the electrochemical properties of $Mg_{2/3}Ni_{4/3}O_2$ rocksalt particles with Maxsorb MSC-30 as counter/reference electrodes and with 1 M ($Mg(TFSA)_2$) in adiponitrile as the electrolyte, tested at 70 °C. Fig. 6c shows the typical charge and discharge curves of $Mg_{2/3}Ni_{4/3}O_2$ nanoparticles at current rate of C/50 with cut-off voltage window of −1.5 to 1.0 V *vs.* carbon. The charge curves show an increase in potential from −1.5 to 1.0 V *vs.* carbon with charge capacities up to 72.0 mA h g^{-1}. The discharge curves of the electrode possess average voltage of *ca.* 2.0 V *vs.* Mg/Mg^{2+}, which is moderate among cathode materials of magnesium battery. The $Mg_{2/3}Ni_{4/3}O_2$ nanoparticles exhibited a initial discharge capacity of 63.9 mA h g^{-1}, which are comparable to the reported values by Ichitsubo *et al.*[31] Fig. 6d displays the cycling test of the $Mg_{2/3}Ni_{4/3}O_2$ nanoparticles. The specific capacity decreased continuously cycle by cycle to 38.0 mA h g^{-1} after 30 cycles. At the 10th cycle and 20th cycles, the discharge capacities are 50.2 and 43.1 mA h g^{-1}, corresponding to the extraction of 0.19 and 0.16 Mg atoms per formula unit, respectively. The capacities reduce quickly due to the transformation from spinel to rocksalt phase (Fig. 7). During the electrochemical cycling, the average coulombic efficiencies decreased and increased again to reach 99% (Fig. 6d). This phenomena correlates with the formation of solid-interface electrolytes in initial 10 cycles. The electrochemical cycling develop and stabilize this solid-interface electrolytes and the system reaches charge and mass balance, result in the stable coulombic efficiency after 20 cycles.

Among the intercalation compounds, disordered rocksalt materials are able to provide high capacities for Li-ion batteries thank to the percolation of a certain type of active diffusion channels.[37,38] In the magnesium rocksalt compound, the magnesium may diffuse by hopping from one octahedral site to another octahedral site *via* an intermediate tetrahedral site. It has been clearly confirmed that, even layered oxides was initially used, it tend to transfer to rocksalt disordered oxides during the cycling, by direct observation by advanced electron microscopy and spectroscopy analysis.[37] And the disordered rocksalt materials can act as high-performance intercalation battery electrode afterward. In our material, the phase transition from spinel to rocksalt during the Mg^{2+} ion intercalation has been confirmed by HRTEM (Fig. 7). Thus, the study on Mg–M–O rocksalt materials are merits for future development of Mg-ion batteries.

4. Conclusions

In summary, spinel-type $MgCo_2O_4$ and rocksalt-type $Mg_{2/3}Ni_{4/3}O_2$ crystalline nanocrystals have been synthesized by rapid supercritical fluid water. The synthesis is facile and rapid and their resultant small crystallite size with short Mg diffusion length may enhance fast charge and mass transport as well as enhancing the contact with the electrolyte and the resulting reaction kinetics. The $MgCo_2O_4$ and $Mg_{2/3}Ni_{4/3}O_2$ nanoparticles were used as cathode materials for magnesium batteries, and the cells exhibited discharge capacities up to 124.1 and 69.8 mA h g^{-1}, respectively. Our study emphasizes on the effect of synthetic method and resulting particle morphology on electrochemical properties, paving a way toward boosting electrode performance for magnesium ion batteries.

Conflicts of interest

There are no conflicts of interest to declare.

Acknowledgements

This research work was financially supported by Japan Society for Promotion of Science for postdoctoral research fellow (JSPS, Pathway to University Position in Japan, Grant No. PU15903), and through a “Grant-in-Aid for Scientific Research” & “Grant-in-Aid for Challenging Exploratory Research” funding programs.

Notes and references

1 P. Canepa, G. Gautam, D. Hannah, R. Malik, M. Liu, K. Gallagher, K. Persson and G. Ceder, *Chem. Rev.*, 2017, **117**, 4287–4341.
2 D. Wang, X. Gao, Y. Chen, L. Jin, C. Kuss and P. G. Bruce, *Nat. Mater.*, 2018, **17**, 16–20.
3 M.-C. Lin, M. Gong, B. Lu, Y. Wu, D.-Y. Wang, M. Guan, M. Angell, C. Chen, J. Yang, B.-J. Hwang and H. Dai, *Nature*, 2015, **520**, 324–328.
4 D. Aurbach, Z. Lu, A. Schechter, Y. Gofer, H. Gizbar, R. Turgeman, Y. Cohen, M. Moshkovich and E. Levi, *Nature*, 2000, **407**, 724–727.
5 L. F. Wan and D. Prendergast, *J. Am. Chem. Soc.*, 2014, **136**, 14456–14464.
6 T. J. Carter, R. Mohtadi, T. S. Arthur, F. Mizuno, R. Zhang, S. Shirai and J. W. Kamp, *Angew. Chem., Int. Ed.*, 2014, **53**, 3173–3177.
7 R. E. Doe, R. Han, J. Hwang, A. J. Gmitter, I. Shterenberg, Y. H. Yoo, N. Pour and D. Aurbach, *Chem. Commun.*, 2014, **50**, 243–245.
8 Z. D. Huang, T. Masese, Y. Orikasa, T. Mori, T. Minato, C. Tassel, Y. Kobayashi, H. Kageyama and Y. Uchimoto, *J. Mater. Chem. A*, 2014, **2**, 11578–11582.
9 N. Singh, T. S. Arthur, C. Ling, M. Matsui and F. Mizuno, *Chem. Commun.*, 2012, **49**, 149–151.
10 Y. S. Guo, F. Zhang, J. Yang, F. F. Wang, Y. NuLi and S. I. Hirano, *Energy Environ. Sci.*, 2012, **5**, 9100–9106.
11 T. Gao, M. Noked, A. J. Pearse, E. Gillette, X. Fan, Y. Zhu, C. Luo, L. Suo, M. Schroeder, K. Xu, S. B. Lee, G. W. Rubloff and C. Wang, *J. Am. Chem. Soc.*, 2015, **137**, 12388–12393.
12 K. R. Chemelewski, D. W. Shin, W. Li and A. Manthiram, *J. Mater. Chem. A*, 2013, **1**, 3347.
13 K. R. Chemelewski, W. Li, A. Gutierrez and A. Manthiram, *J. Mater. Chem. A*, 2013, **1**, 15334–15341.

14 J. Ma, P. Hu, G. Cui and L. Chen, *Chem. Mater.*, 2016, **28**, 3578–3606.

15 Y. Luo, Y. Zhang, L. Yan, J. Xie and T. Lv, *ACS Appl. Mater. Interfaces*, 2018, **10**, 31795–31803.

16 G. Liu, Q. G. Chi, Y. Q. Zhang, Q. Q. Chen, C. H. Zhang, K. Zhu and D. X. Cao, *Chem. Commun.*, 2018, **54**, 9474–9477.

17 S. Tao, W. F. Huang, Y. S. Liu, S. M. Chen, B. Qian and L. Song, *J. Mater. Chem. A*, 2018, **6**, 8210–8214.

18 J. Yin, A. B. Brady, E. S. Takeuchi, A. C. Marschilok and K. J. Takeuchi, *Chem. Commun.*, 2017, **53**, 3665–3668.

19 L. Hu, I. D. Johnson, S. Kim, G. M. Nolis, J. W. Freeland, H. D. Yoo, T. T. Fister, L. McCafferty, T. E. Ashton, J. A. Darr and J. Cabana, *Nanoscale*, 2019, **11**, 639–646.

20 R. Dinesh, M. K. Devaraju, T. Tomai, A. Unemoto and I. Honma, *Nano Lett.*, 2012, **12**, 1146–1151.

21 Q. D. Truong, M. K. Devaraju, Y. Ganbe, T. Tomai and I. Honma, *Sci. Rep.*, 2014, **4**, 3975.

22 Q. D. Truong, M. K. Devaraju and I. Honma, *J. Mater. Chem. A*, 2014, **2**, 17400–17407.

23 M. K. Devaraju, D. Rangappa and I. Honma, *Chem. Commun.*, 2012, **48**, 2698–2700.

24 Q. D. Truong, M. K. Devaraju and I. Honma, *J. Power Sources*, 2017, **361**, 195–202.

25 Q. D. Truong, M. K. Devaraju, D. N. Nguyen, Y. Gambe, K. Nayuki, Y. Sasaki, P. D. Tran and I. Honma, *Nano Lett.*, 2016, **16**, 5829–5835.

26 G. Gershinsky, H. D. Yoo, Y. Gofer and D. Aurbach, *Langmuir*, 2013, **29**, 10964–10972.

27 X. Q. Sun, V. Duffort, B. L. Mehdi, N. D. Browning and L. F. Nazar, *Chem. Mater.*, 2016, **28**, 534.

28 Q. D. Truong, M. K. Devaraju, Y. Gambe, K. Nayuki, Y. Sasaki, P. D. Tran and I. Honma, *Chem. Mater.*, 2017, **29**, 6245–6251.

29 R. A. Quinlan, Y.-C. Lu, Y. Shao-Horn and A. N. Mansour, *J. Electrochem. Soc.*, 2013, **160**, A669–A677.

30 A. N. Mansour, *Surf. Sci. Spectra*, 1994, **3**, 231–238.

31 T. Ichitsubo, T. Adachi, S. Yagi and T. Doi, *J. Mater. Chem.*, 2011, **21**, 11764.

32 S. Okamoto, T. Ichitsubo, T. Kawaguchi, Y. Kumagai, F. Oba, S. Yagi, K. Shimokawa, N. Goto, T. Doi and E. Matsubara, *Adv. Sci.*, 2015, **2**, 1500072.

33 T. Ichitsubo, S. Okamoto, T. Kawaguchi, Y. Kumagai, F. Oba, S. Yagi, N. Goto, T. Doi and E. Matsubara, *J. Mater. Chem. A*, 2015, **3**, 10188–10194.

34 Y. Kotani, R. Ise, K. Ishii, T. Mandai, Y. Oaki, S. Yagi and H. Imai, *J. Alloys Compd.*, 2018, **739**, 793–798.

35 K. Shimokawa, H. Matsumoto and T. Ichitsubo, *J. Phys. Chem. Lett.*, 2018, **9**(16), 4732–4737.

36 N. Kitamura, Y. Tanabe, N. Ishida and Y. Idemoto, *Chem. Commun.*, 2019, **55**, 2517–2520.

37 J. Lee, A. Urban, X. Li, D. Su, G. Hautier and G. Ceder, *Science*, 2014, **343**, 519–522.

38 M. Freire, N. V. Kosova, C. Jordy, D. Chateigner, O. I. Lebedev, A. Maignan and V. Pralong, *Nat. Mater.*, 2016, **15**, 173.